Nanoscale

Accepted Manuscript

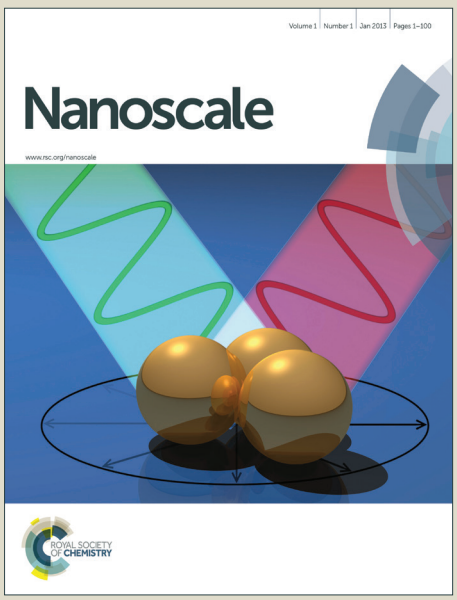

ROYAL SOCIETY OF CHEMISTRY

www.rsc.org/nanoscale

Journal Name

RSCPublishing

ARTICLE

Enhanced photocatalytic performances of n-TiO_2 nanotubes by uniform creation of p-n heterojunctions with p-Bi_2O_3 quantum dots

Cite this: DOI: 10.1039/xoxxoooooox

Received ooth January 2012,
Accepted ooth January 2012

DOI: 10.1039/xoxxoooooox

www.rsc.org/

Ming-Zheng Ge,[‡a] Chun-Yan Cao,[‡a] Shu-Hui Li,[a] Song-Nan Zhang,[a] Shu Deng,[a] Jian-Ying Huang,*[a] Qing-Song Li,[a] Ke-Qin Zhang,*[a,b] Salem S. Al-Deyab[c] and Yue-Kun Lai*[a,b]

An ultrasonication-assisted successive ionic layer adsorption and reaction (SILAR) strategy was developed to uniformly deposit high density p-type Bi_2O_3 quantum dots on n-type TiO_2 nanotube arrays (Bi_2O_3@TiO_2 NTAs), which were constructed by electrochemical anodizing in ethylene glycol containing electrolyte. Compared with pristine TiO_2 NTAs, the Bi_2O_3 quantum dots sensitized TiO_2 NTAs exhibited highly efficient photocatalytic degradation of methyl orange (MO). The kinetic constant of Bi_2O_3@TiO_2 NTAs prepared by an ultrasonication-assisted SILAR process of 4 cycles was 1.95 times higher than that of the pristine TiO_2 NTAs counterpart. The highly efficient photocatalytic activity is attributed to the synergistic effect between the formation of uniform p-n heterojunction with a high-density for enhancing light absorption and facilitating photogenerated electron-hole separation/transfer. The results suggest that Bi_2O_3/TiO_2 p-n heterojunction nanotube arrays are very promising for enhancing the photocatalytic activity and open up a promising strategy to design and construct high efficiency heterogeneous semiconductor photocatalysts.

Titanium dioxide (TiO_2), since discovered on water photolysis by Fujishima and Honda in 1972,[1] has been paid much attention and widely used in photocatalytic degradation of organic pollutants,[2] dye-sensitized solar cells,[3] biomedical materials,[4] sensor/detector[5] and hydrogen production by splitting water[6] because of its low cost, good mechanical properties and high biocompatibility.[7] Compared to TiO_2 nanoparticles and nanowires, vertically aligned TiO_2 NTAs on Ti substrate by electrochemical anodizing have been paid more attention due to the oriented charge transfer channel, the large interfacial area, and especially lower recombination rate of photogenerated electrons and holes.[8] However, associated with wide band gap (anatase: 3.2 eV, rutile: 3.0 eV) and the fast recombination of photogenerated electron-hole pairs, the wide application of TiO_2 NTAs was limited in some fields.

In recent years, in order to enhance the photocatalytic activity of TiO_2 NTAs, a lot of materials were used to modify TiO_2 NTAs by suppressing the recombination of photogenerated electrons-hole pairs and improving the transport of photocarriers, such as metal (Ag, Au, Pt and Pd),[9] non-metal (N, C, F and S),[10] semiconductor (CdS, Cu_2O and NiO).[11] Especially, the formation of p-n heterojunctions is thought to be one of the most effective strategies to enhance the photocatalytic activity due to the existence of an internal electric field in the interface.[12] Therefore, it is urgent to search for novel heterostructured materials to couple with TiO_2 NTAs in material chemistry.

Bismuth oxide (Bi_2O_3), as a p-type semiconductor, has been extensively used in gas sensors,[13] photoelectric coatings[14] and catalysts[15] because of high refractive index, high dielectric permittivity and photoluminescence properties.[16] There are six polymorphs phase of Bi_2O_3: α-Bi_2O_3 (monoclinic), β-Bi_2O_3 (tetragonal), γ-Bi_2O_3 (b.c.c.), δ-Bi_2O_3 (f.c.c.), ε-Bi_2O_3 (orthorhombic) and w-Bi_2O_3 (triclinic).[17] Among them, β-Bi_2O_3 has excellent advantages and demonstrates appreciable properties for decomposing pollutants.[18] It has a narrower band gap of about 2.8 eV and can decrease the band gap of TiO_2.[19] Since TiO_2 is a well-known n-type semiconductor, it is promising to decorate TiO_2 with p-Bi_2O_3 to enhance the photocatalytic efficiency because the formation of p-n junctions can markedly facilitate the separation of electron and hole.[28] Recently, there are some reports about Bi_2O_3/TiO_2 composite nanotube arrays synthesized by an electrochemical method and electrophoretic deposition,[20] but these techniques exhibit poor control over the particle size and distribution.

Herein, we present an ultrasonication-assisted successive ionic layer adsorption and reaction (SILAR) technique to uniformly deposit Bi_2O_3 quantum dots on vertically aligned TiO_2 NATs with a high density. The morphology, structure and photoelectrochemical

performance of TiO_2 NTAs with or without Bi_2O_3 quantum dots loading were systematically investigated and discussed. Compared to pristine TiO_2 NTAs, the Bi_2O_3@TiO_2 NTAs p-n heterojunction exhibited the synergistic effect between enhanced light adsorption capacity of specific composite structure and facilitated the photogenerated charges separation/transfer of novel p-n heterojunction. The photocatalytic activity of Bi_2O_3-TiO_2 NTAs p-n heterojunction was evaluated by the photocatalytic degradation of methyl orange aqueous solutions.

Experimental

Preparation of anodized TiO_2 NTAs: Prior to anodization, titanium foils were ultrasonically cleaned in acetone and ethanol for 30 minutes, respectively. Then cleaned Ti foils (3.0 × 1.5 cm^2) was anodized at room temperature in a conventional two-electrode cell with Pt as counter electrode in ethylene glycol containing 0.5 wt% NH_4F and 2 vol% H_2O. Subsequently, the 50 V potential was applied for 2h for the growth of nanotube arrays. Rinsed with distilled water, the as anodized Ti foils was then ultrasonically rinsed in ethanol for 5 minutes. At last, the samples were rinsed in distilled water and dried in air. The as-prepared amorphous TiO_2 nanotube arrays were annealed in air at 400°C for 2 h with a heating rate and cooling rate of 5°C/min to convert to crystalline phases.

Preparation of Bi_2O_3@TiO_2 NTAs: Bi_2O_3 quantum dots were loaded onto both the outer and inner walls of TiO_2 nanotubes by the ultrasonication-assisted successive ionic layer adsorption and reaction (SILAR) technique. Typically, the annealed TiO_2 NTAs were immersed successively in 5 mM $Bi(NO_3)_3$•$5H_2O$ ethylene glycol solution and 0.1 M NaOH ethanol solution for 10 minutes, respectively, and simultaneously assisted with a ultrasound frequency of 40 kHz by using an ultrasonic generator (KQ100E, Kunshan Ultrasonic Instrument Co., Ltd). Between each immersion step, the samples were rinsed with ethanol adequately to remove excess ions. Such operation process was repeated for 1 to 7 cycles. The corresponding samples were marked as Bi_2O_3@TiO_2 NTAs-1 to Bi_2O_3@TiO_2 NTAs-7, respectively. The samples were rinsed with ethanol and dried in air, then annealed in air at 450°C for 2 h with a heating rate and cooling rate of 5°C/min. The procedures for the preparation of Bi_2O_3@TiO_2 NTAs are illustrated in Scheme 1.

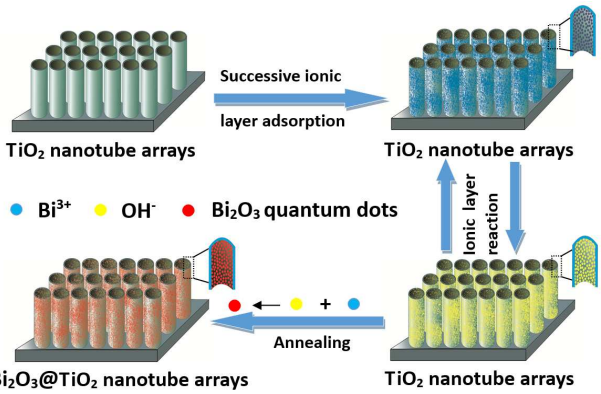

Scheme 1. Schematic diagram of the procedures for preparation of Bi_2O_3@TiO_2 NTAs.

Characterization of Bi_2O_3@TiO_2 NTAs: The structure and morphology of Bi_2O_3@TiO_2 NTAs were characterized by a field emission scanning electron microscope (SEM, Hitachi-S4800). The microstructures, compositions and the presence of Bi_2O_3 were further confirmed by using a transmission electron microscopy (TEM, FEI Tecnai G-20 operated at 200 kV). Energy dispersive X-ray (EDX) spectrometer fitted to the TEM was applied for elemental analysis. The crystal phases were identified by an X-ray diffractometer with Cu-Ka radiation (XRD, Philips, X´pert-Pro MRD). X-ray photoelectron spectroscopy (XPS, KRATOS, Axis Ultra HAS) was employed to analyze the chemical component and the concentration of atoms of Bi_2O_3@TiO_2 NTAs. The binding energies were normalized to the signal for adventitious C 1s at 284.5 eV. UV-Vis diffuse reflection spectroscopy (UV-DRS) was recorded in range of 250-800 nm at room temperature by using UV-3600 spectrophotometer. Photoluminescence (PL) measurements were carried out at room temperature by using fluorescence spectroscopy (made by HOKIBA JOBIN YVON, FM4P-TCSPC) with a Xenon lamp as excitation source (λ_{ex} = 370 nm).

Photoelectrochemical measurements: The photocurrent measurement and electrochemical impedance spectroscopy (EIS) measures were carried out in a quartz beaker using an electrochemical workstation (CHI 660D) in a standard three-electrode configuration with TiO_2 NTAs, Bi_2O_3@TiO_2 NTAs electrode as the working electrode. The counter and reference electrodes were Pt wire and saturated calomel electrode (SCE), respectively. A 0.1 M Na_2SO_4 aqueous solution was used as the electrolyte. The area of working electrodes was 3.0 cm^2. The working electrode was irradiated with a GY-10 xenon lamp during the measurement. The distance between the window of the flask and light source was 15 cm. The focused incident light intensity on the flask was ca. 100 mW/cm^2. The EIS measurements were performed to scrutinize the interfacial properties between the electrode (i.e., TiO_2 NTAs, Bi_2O_3@TiO_2 NTAs) and the electrolyte over a frequency range from 1 × 10^3 Hz to 0.1 Hz with a low open circuit potential both in the dark and under solar light illumination.

Photocatalytic measurements: The photocatalytic activity of Bi_2O_3@TiO_2 NTAs was evaluated by the degradation of MO pollutant solution with an initial concentration of 10 mg/L (pH = 8.5). A 300 W mercury lamp was used as the simulated ultraviolet light source. The distance between the samples was 8 cm. Before light irradiation, the samples were immersed with 15 ml MO aqueous solution in quartz reactor at room temperature for 1 h to establish adsorption equilibrium. The reactor was equipped with a water jacket to control the reaction temperature. The concentration of MO was analyzed with a 30 min interval by using UV-Vis spectrophotometer (Hitachi, UV-1080, Japan) at wavelength of 463 nm.

Results and discussion

Figure 1a,b showed the FESEM images of TiO_2 NTAs. The TiO_2 NTAs demonstrated a high density, well-ordered and uniform tubular structure with a length of 4-6 μm and an average pore diameter of 90-100 nm. Figure 1c-f displayed the

SEM images of TiO_2 NTAs with ultrasonication-assisted SILAR deposition for 1, 4 and 7 cycles, respectively. A little amount of Bi_2O_3 quantum dots were deposited on the surface and inner walls of TiO_2 NTAs and were dispersed mainly around the nanotube entrance with one single cycle (Figure 1c). With the increase of SILAR cycles, the amount of Bi_2O_3 quantum dots on nanotube is also markedly increased. As SILAR processes were up to 4 cycles, the Bi_2O_3 quantum dots with an average size of about 10 nm were uniformly deposited on the top of TiO_2 nanotubes (Figure 1d). The corresponding cross-sectional SEM image (Figure 1e) showed that a lot of Bi_2O_3 quantum dots were well distributed on both outside and inside TiO_2 nanotube walls. When the SILAR process increases up to 7 cycles, the average size of Bi_2O_3 nanoparticles increases significantly to 25 nm, which leads to the obvious increase of wall thickness and decrease of nanotube inner diameter (Figure 1f). Figure S1† shows the size of Bi_2O_3 quantum dots and mass ratios of Bi, O, Ti with multiple SILAR processes for 1, 4, 7 cycles, respectively. With the increase of SILAR cycles ranging from 1 to 7 cycles, the mass ratio of Bi element increased from 0.46% to 2.99%, respectively. Obviously, such ultrasonication-assisted SILAR process can effectively suppress the aggregation of the Bi_2O_3 quantum dots on nanotube entrance, and will not destroy the highly ordered tubular structure of TiO_2 NTAs.

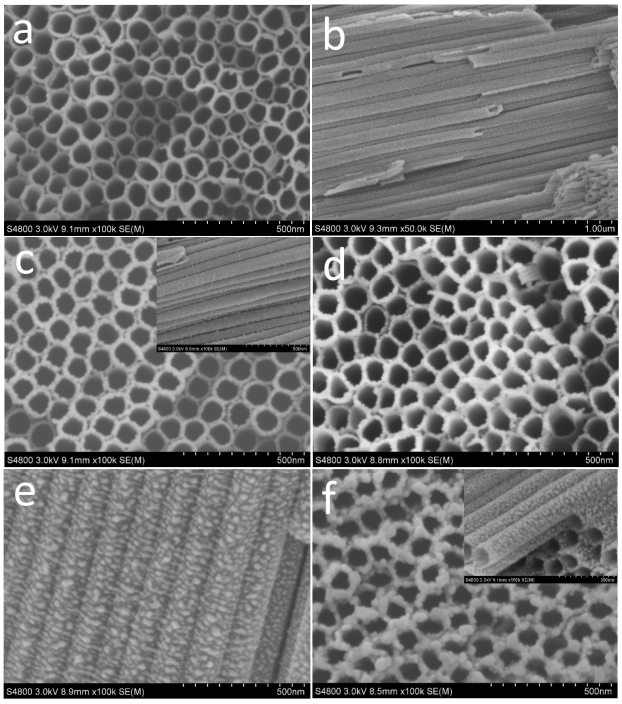

Figure 1. Typical top-view (a) and side-view (b) SEM images of the pure TiO_2 NTAs, SEM images of Bi_2O_3@TiO_2 NTAs with SILAR processes for 1 cycle (c), top-view (e) and side-view (f) SEM images of Bi_2O_3@TiO_2 NTAs with multiple SILAR processes for 4 cycles, SEM images of Bi_2O_3@TiO_2 NTAs with multiple SILAR processes for 7 cycles (f).

The TEM image of the as-synthesized Bi_2O_3@TiO_2 NTAs sample showed that Bi_2O_3 quantum dots were uniformly deposited on and inside TiO_2 nanotubes (Figure 2a,b). Figure 2c presented a typical high resolution TEM image of the selected area marked in Figure 2a, which revealing a uniform distribution of Bi_2O_3 quantum dots on the nanotube with small particle size. The lattice fringes of 0.352 nm and 0.321 nm corresponded to the reflections from the (101) plane of anatase TiO_2 and (221) plane of β-Bi_2O_3, respectively. The EDX spectrum (Figure 2d) and corresponding element mapping (Figure 2e) of single nanotube demonstrate that the as-prepared Bi_2O_3 quantum dots is uniform and highly dispersed on TiO_2 nanotube. Except for Ti, O element, the Bi_2O_3@TiO_2 NTAs sample with 4 cycles of SILAR processes has an atomic percentage of Bi about 1.14%. In comparison to the uniform distribution of Ti and O sourced from TiO_2 substrate, the mapping of Bi exhibited an evenly distributed dot pattern, indicating that Bi_2O_3 quantum dots were uniformly anchored on and inside TiO_2 nanotubes. Figure S2† shows the TEM images of pristine TiO_2 nanotube arrays. After deposition Bi_2O_3 quantum dots, the wall thickness of Bi_2O_3@TiO_2 NTAs increased and the tubes became opaque.

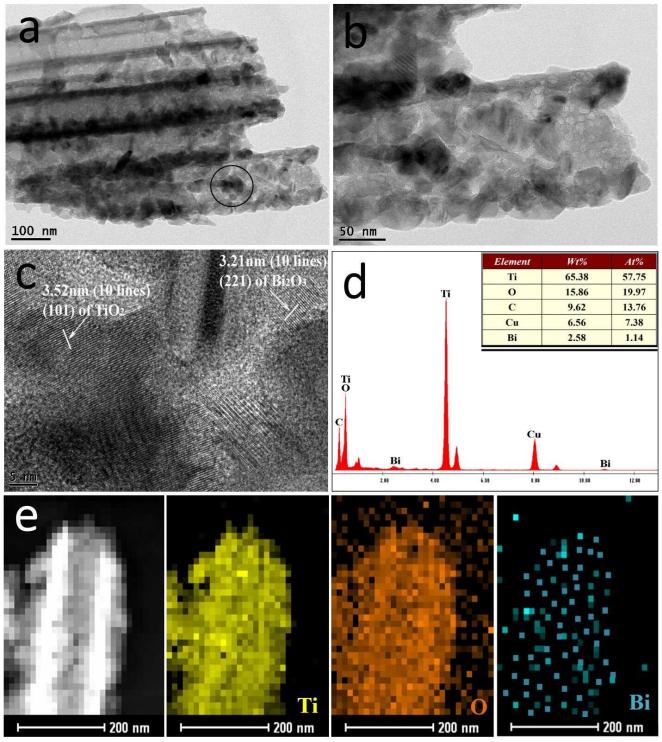

Figure 2. (a,b) Low magnified TEM image of Bi_2O_3@TiO_2 NTAs fabricated by an ultrasonication-assisted SILAR process of 4 cycles; (c) The high resolution TEM image of the selected area marked in (a); (d) EDX spectrum of Bi_2O_3@TiO_2 NTAs sample; (e) EDX mapping of a single TiO_2 nanotube loaded with uniform Bi_2O_3 quantum dots.

Figure 3a presented the XRD patterns of the TiO_2 NTAs with or without the deposition of Bi_2O_3 quantum dots. The diffraction peaks at 25.3°, 37.9°, 48.0° and 53.9° of pristine

TiO_2 NTAs could be well indexed to the (101), (004), (200) and (105) planes of TiO_2 anatase phase (JCPDS no. 21-1272). After Bi_2O_3 deposition, due to the well dispersed and small size Bi_2O_3 quantum dots, there is a low intensity peak at 27.9° and 31.8° in accordance with a standard diffraction of β-Bi_2O_3 (JCPDS no. 29-0236), corresponding to the (221) plane and (002) plane of β-Bi_2O_3, which is consistent with the results of TEM.[21] The raman spectra of TiO_2 NTAs and Bi_2O_3@TiO_2 NTAs were showed in Figure 3b. The characteristics peaks of pristine TiO_2 NTAs at 144, 197, 395, 513 and 634 cm^{-1} are attributed to Raman-active modes of anatase TiO_2.[22] When doping with Bi_2O_3 quantum dots, the obvious peaks of Bi_2O_3@TiO_2 NTAs appeared at 229, 307 cm^{-1} because of internal stretching modes of Bi-O bonds with the various bond lengths,[23] indicating that β-Bi_2O_3 quantum dots were deposited on TiO_2 NTAs successfully.

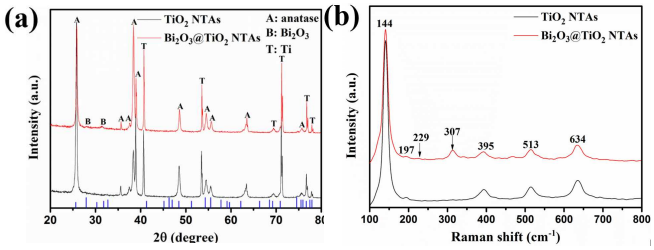

Figure 3. XRD (a) and Raman spectra (b) of Bi_2O_3@TiO_2 NTAs with SILAR processes for 4 cycles, TiO_2 NTAs at 400°C and standard JCPDS data for β-Bi_2O_3 (blue short bars in (a)).

The chemical component of Bi_2O_3@TiO_2 NTAs was analyzed by XPS. Figure 4a,b showed XPS survey spectrum of TiO_2 NTAs and Bi_2O_3@TiO_2 NTAs, respectively. It can be seen that except for the O 1s (532.4 eV), Ti 2p (458.9 eV) and C 1s (284.5 eV) peaks, peaks such as Bi 4d and Bi 4f, emerged with strong relative intensities, indicating that TiO_2 NTAs were mainly coated with Bi_2O_3 quantum dots (Figure 4b). The C 1s peak is ascribed to adventitious hydrocarbon from the XPS instrument itself. The higher resolution XPS spectrum of the Bi 4f region is displayed in Fig. 4c. The Bi 4f XPS spectra were fitted into two peaks at 158.4 eV (Bi $4f_{7/2}$) and 163.8 eV (Bi $4f_{5/2}$). The binding energy between Bi $4f_{7/2}$ and Bi $4f_{5/2}$ is approximately 5.4 eV, showing the +3 valence state of Bi element, which indicated the existence of Bi_2O_3.[24] Figure 4d showed the high resolution XPS spectrum of O 1s. The oxygen on the sample surface existed in the form of the binding energies of 532.0, 530.2 and 529.5 eV.[25] The main peaks at 530.0 eV and 529.5 eV could be ascribed to the O lattice of TiO_2 and Bi_2O_3 quantum dots, respectively. The peak at 532.2 eV is attributed to irreversibly adsorbed water molecules on the surface of the Bi_2O_3@TiO_2 NTAs sample.[26]

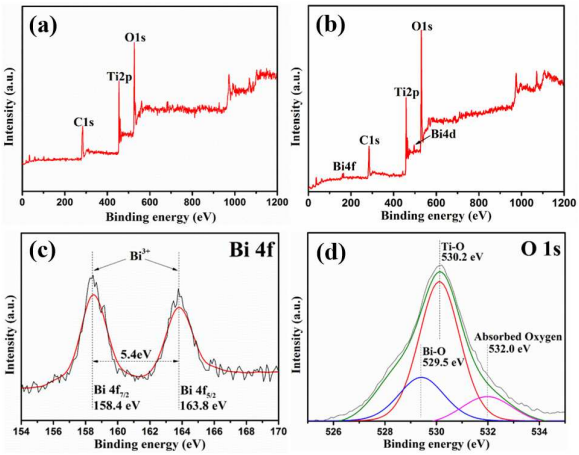

Figure 4. Survey XPS spectrum of TiO_2 NTAs (a) Bi_2O_3/TiO_2 NTAs with a SILAR process of 4 cycles (b) and corresponding high resolution XPS spectra of Bi 4f (c) and O 1s (d) of Bi_2O_3@TiO_2 NTAs.

Figure 5a displayed the UV-Vis diffuse reflectance spectra (UV-DRS) of TiO_2 NTAs and Bi_2O_3/TiO_2 NTAs with different SILAR processes. The pristine TiO_2 NTAs showed an absorption band lower than 390 nm due to the charge from O 2p valance band to Ti 3d conduction band.[27] Compared to pristine TiO_2 NTAs, the Bi_2O_3@TiO_2 NTAs-1, 4 and 7 exhibit a broader and stronger absorption in both UV and visible light regions. The band edges of the samples were approaching the visible-light region owing to the synergistic effect of Bi_2O_3 photosensitizing and the creation of p-n heterojunction.[28] Moreover, the Bi orbit may be essential to decrease the energy gap between Ti and O orbitals of Ti oxide to enable the red shift.[29] Usually, the higher absorption toward visible region verified the better photocatalytic activity of photocatalysis. Therefore, the Bi_2O_3/TiO_2 NTAs-4 possessed the strongest absorption among all samples, and thus the highest photocatalytic activity was expected. Figure 5b showed the PL spectra of TiO_2 NTAs and Bi_2O_3@TiO_2 NTAs with different SILAR processes. Due to the oxygen vacancy of TiO_2 NTAs, the peaks appeared at about 452 nm, 471 nm, 490 nm and 595 nm.[30] The lower PL intensity signified that the separation and transfer efficiency of photogenerated electron-hole pairs was stronger and thus a higher photocatalytic activity yield. Compared with pristine TiO_2 NTAs, Bi_2O_3@TiO_2 NTAs displayed lower PL intensity. The PL intensity decreases in the order of Bi_2O_3@TiO_2 NTAs-4 < Bi_2O_3@TiO_2 NTAs-1 < Bi_2O_3@TiO_2 NTAs-7 < pure TiO_2 NTAs. The increase in the PL signal of the samples obtained with longer SILAR cycles (i.e., Bi_2O_3/TiO_2 NTAs-7) suggested that the larger Bi_2O_3 quantum dots and nanoclusters may act as the charge recombination center, rather than facilitate electron-hole separation, and partially block the channels of TiO_2 nanotubes. These results indicated that the presence of Bi_2O_3 quantum dots with optimized size and uniform distribution would decrease the recombination of electron-hole pairs to endow Bi_2O_3@TiO_2 NTAs-4 with the best photochemical activity. Figure S3† shows the time-resolved photoluminescence (TRPL) spectrum of TiO_2 NTAs and Bi_2O_3@TiO_2 NTAs with ultrasonication-assisted SILAR deposition for 1, 4 and 7 cycles. Compared to the pristine

TiO_2 NTAs, Bi_2O_3@TiO_2 NTAs displayed longer decay lifetime. Longer decay lifetime clearly indicates lower recombination and higher separation efficiency of electron-hole pairs.[31] What's more, lower recombination of electron-hole pairs will lead to weaker photoluminescence and higher photocatalytic activity, which is consistent with the PL spectra. Bi_2O_3@TiO_2 NTAs with ultrasonication-assisted SILAR deposition for 4 cycles owns the longest decay lifetime and the highest photocatalytic activity.

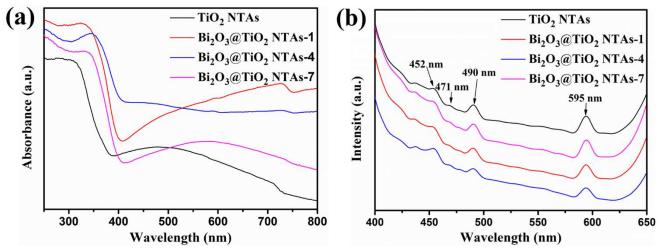

Figure 5. UV-DRS spectra (a) and PL spectra (b) of pristine TiO_2 NTAs and Bi_2O_3@TiO_2 NTAs with different SILAR processes for 1, 4, and 7 cycles.

The separation of photogenerated electron-hole pairs was evaluated by measuring the photocurrent. Figure 6 showed the current-time (I-t) characteristics of pure TiO_2 NTAs and Bi_2O_3@TiO_2 NTAs-1, 4 and 7 electrodes recorded in 0.1 M Na_2SO_4 under simulated solar irradiation. As shown in Figure 6, when the pristine TiO_2 NTAs electrode was under light irradiation, there was a photocurrent density with ca. 0.09 mA/cm^2. However, the photocurrent density of the Bi_2O_3/TiO_2 NTAs with different SILAR processes for 1, 4 and 7 cycles was 0.43 mA/ cm^2, 0.51 mA/cm^2, 0.19 mA/cm^2, which was approximately 4.8 times, 5.8 times, 2.1 times higher than that of TiO_2 NTAs electrode, respectively. The enhanced photocurrent could be ascribed to the decoration of Bi_2O_3 quantum dots into the TiO_2 NTAs system, resulting in faster electron transport from the valance band to the conduction band of TiO_2 and higher separation efficiency of photogenerated electron-hole pairs.[32]

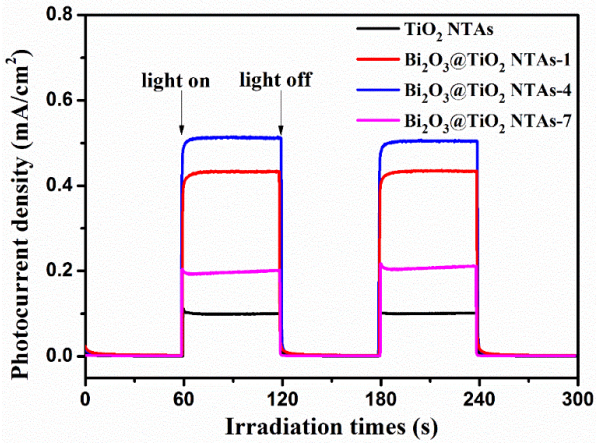

Figure 6. Photocurrent responses of as-prepared pristine TiO_2 NTAs and Bi_2O_3/TiO_2 NTAs with different SILAR processes for 1, 4, and 7 cycles under UV irradiation in 0.1 M Na_2SO_4 solution recorded at 1.0 V. The illumination from a 150 W Xe lamp was interrupted every 60 s.

The electrochemical impedance spectroscopy (EIS) measurements were an effective tool for scrutinizing the interfacial properties between the electrode (i.e., TiO_2 NTAs annealed at 450°C and Bi_2O_3@TiO_2 NTAs-4 at 450°C) and the electrolyte. The diameter of semicircle in the Nyquist plots at high frequency reflects the charge transfer process, and the smaller diameter of semicircle represents the lower charge transfer resistance.[33] As shown in Figure 7, the diameters of TiO_2 NTAs at 450°C were much larger than those of Bi_2O_3@TiO_2 NTAs-4 in the dark as well as under simulated solar light irradiation. This supported that the Bi_2O_3 quantum dots decoration considerably reduced the recombination of electron-hole pairs and enhanced photocatalytic activity. Figure S4† shows the Bode phase plots of TiO_2 NTAs and Bi_2O_3@TiO_2 NTAs-4 under simulated solar light irradiation. The electron lifetime in photonode is correlated with the characteristic frequency peaks in Bode phase plots. The longer electron lifetimes revealed longer electron migration distance with fewer trappings and lower combination of electron-hole pairs. Compared to pristine TiO_2 NTAs, Bi_2O_3@TiO_2 NTAs-4 displayed a little longer electron lifetimes. These results suggest the presence of Bi_2O_3 quantum dots can prolong the electron lifetimes and facilitate the charge transport.[34]

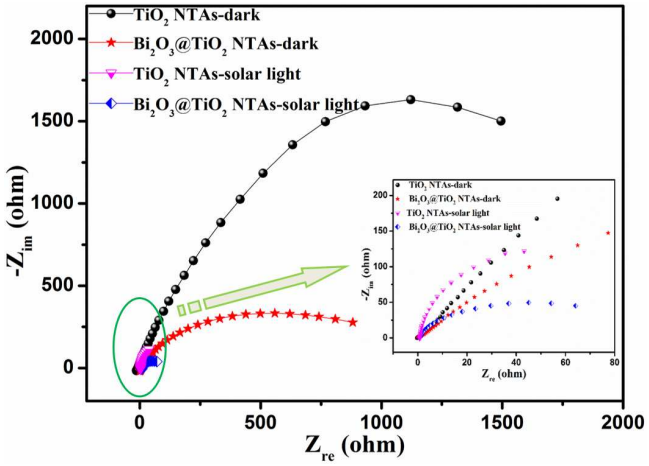

Figure 7. Electrochemical impedance spectra of TiO_2 NTAs at 450°C and Bi_2O_3@TiO_2 NTAs with repeated SILAR processes for 4 cycles in the dark and under solar light illumination, respectively.

The photocatalytic activity of the samples was evaluated by degradation of MO under UV irradiation. The decomposition of MO pollutant followed the first-order reaction kinetics, which could be defined as $\ln(C_0/C_t) = kt$, where C_0, C_t, k, t was the initial MO concentration, concentration after certain reaction time, the rate constant and reaction time, respectively. The MO photodecomposition cures and corresponding kinetic rates of self-degradation, pristine TiO_2 NTAs, Bi_2O_3@TiO_2 NTAs with different repeated SILAR processes for 1, 4, and 7 cycles was depicted in Figure 8. When using the pure TiO_2 NTAs as the photocatalyst, the concentration of MO was reduced by 31.1% after 2 h irradiation. However, it was found that the Bi_2O_3@TiO_2 NTAs with different SILAR processes for 1, 4, and 7 cycles displayed that the concentration of MO was reduced by 43.4%, 51.2% and 40.1% respectively, indicating higher degradation rate than pure TiO_2 NTAs (Figure 8a). The reaction constants k for the pristine TiO_2

NTAs and Bi_2O_3@TiO_2 NTAs with multiple SILAR processes for 1, 4, and 7 cycles were calculated 0.00302, 0.00462, 0.00590 and 0.00418 min^{-1}, respectively (Figure 8b). Evidently, the apparent reaction constant of the photocatalytic degradation of MO with the assistance of TiO_2 photocatalyst and the decoration of Bi_2O_3 quantum dots was significantly higher than that of MO self-degradation (0.00132 min^{-1}). The kinetic constants of the optimized Bi_2O_3@TiO_2 NTAs with a SILAR process of 4 cycles for MO degradation (0.00590 min^{-1}) was 1.95 times higher than the pure TiO_2 NTAs counterpart (0.00302 min^{-1}), indicating that the Bi_2O_3 quantum dots sensitized on the TiO_2 NTAs with p-n heterojunction significantly enhanced the photocatalytic activity.

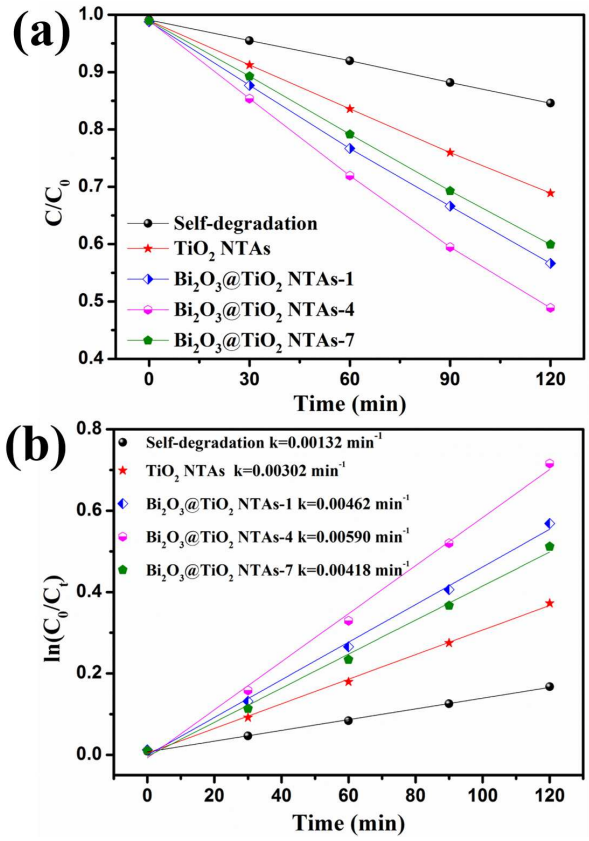

Figure 8. Photodegradation rates of MO for pristine TiO_2 NTAs at 400°C, Bi_2O_3@TiO_2 NTAs with multiple SILAR processes for 1, 4, and 7 cycles.

In addition to the excellent photocatalytic degradation performance, the Bi_2O_3/TiO_2 NTAs with different SILAR processes also exhibited good stability of photocatalytic activity during the degradation process of MO solution. As shown in Figure 9, the MO removal rate of all Bi_2O_3@TiO_2 NTAs with different repeated SILAR processes had a little reduction within 5% after 10 photocatalytic recycling. This indicated that the Bi_2O_3/TiO_2 NTAs remained active for long-term service without obvious deactivation.

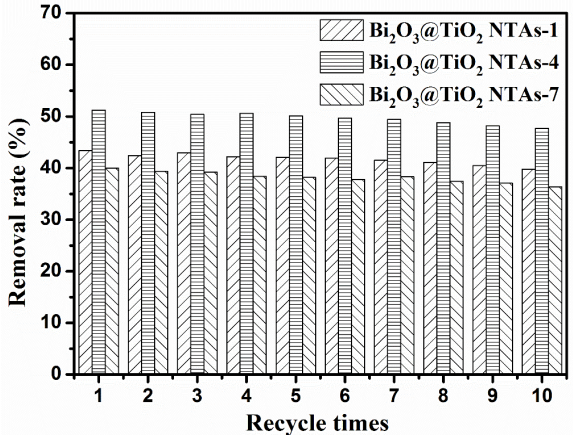

Figure 9. Recycling test of the Bi_2O_3@TiO_2 NTAs with different SILAR processes on the MO removal rate under 2 h of UV light irradiation.

It is believed that the enhanced photocatalytic activity of Bi_2O_3@TiO_2 NTAs is mainly attributed to the p-n heterojunction effect between p-type Bi_2O_3 and n-type TiO_2 heterojunction. In order to describe how Bi_2O_3@TiO_2 NTAs enhanced the photocatalytic activity, the degradation mechanism of MO was illustrated in Scheme 2. The Fermi energy level of n-type TiO_2 lies closer to the conduction band while the Fermi energy level of p-type Bi_2O_3 lies closer to the valence band. When the n-type TiO_2 and p-type Bi_2O_3 formed the p-n heterojunction, it would create the inner electric field between the surface of TiO_2 and Bi_2O_3. During the process, the electrons transfer from Bi_2O_3 to TiO_2 while the holes transfer from TiO_2 to Bi_2O_3 until the system attained equilibration due to the carrier diffusion between the TiO_2 and Bi_2O_3.[33] Under UV irradiation, the photogenerated electron-hole pairs created on the n-type TiO_2 surface are drifted by the electric field in the opposite direction. The holes flow into the negative field and the electrons move to the positive field. Thus, the photoexcited electrons at the conduction band of Bi_2O_3 will move towards the conduction band of TiO_2, and conversely the holes transfer from the valance band of TiO_2 to the valance band of Bi_2O_3 because of the effect of the inner electric field.[35] Therefore, photogenerated electron-hole pairs are separated efficiently and the resultant photocatalytic activity is enhanced. The photocatalytic degradation mechanism of MO is proposed as follows:

$$p\text{-}Bi_2O_3 / n\text{-}TiO_2 + hv \longrightarrow Bi_2O_3(h^+) + TiO_2(e^-)$$

$$TiO_2(e^-) + O_2 \longrightarrow O_2^{\cdot-}$$

$$O_2^{\cdot-} + H_2O \longrightarrow H_2O_2 + {}^{\cdot}OH$$

$$Bi_2O_3(h^+) + H_2O / {-}OH \longrightarrow {}^{\cdot}OH$$

$${}^{\cdot}OH + MO \longrightarrow \text{Degradation}$$

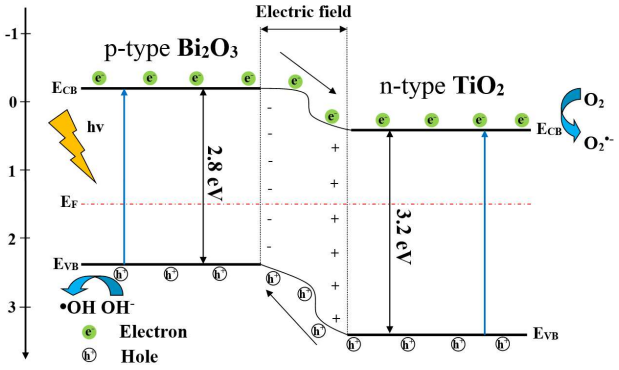

Scheme 2. Schematic diagram showing the energy band structure and electron-hole pairs separation/transfer in the p-type Bi_2O_3/n-type TiO_2 heterojunction under UV irradiation.

Conclusions

In summary, we have developed a very promising strategy of ultrasonication-assisted SILAR processes to realize highly uniform Bi_2O_3 quantum dots dispersed on both inside and outside of the vertically aligned TiO_2 nanotubes. Such novel Bi_2O_3@TiO_2 NTAs p-n heterojunction substantially increased the photogenerated electron-hole separation/transfer, and notably improved photocatalytic activity (1.95 times over the pristine TiO_2 NTAs counterpart), indicating the synergistic effect between the specific nanotube array structure of TiO_2 and uniformly distributed Bi_2O_3 quantum dots facilitating the photoexcited electron transfer from p-type Bi_2O_3 to n-type TiO_2 NTAs for high-efficiency photocatalytic degradation of organic pollutants. Therefore, this study provides an effective synthetic strategy to uniformly synthesize nanoparticle-modified one-dimensional heterostructures which have promising applications in environmental reclamation and energy harvest.

Acknowledgements

The authors thank the Natural Science Foundation of Jiangsu Province of China (BK20130313; BK20140400), National Natural Science Foundation of China (91027039; 51373110). Deanship of Scientific Research at King Saud University (RGP-089). We also acknowledge the funds from the project of the Priority Academic Program Development of Jiangsu Higher Education Institutions (PAPD), Qing Lan Project for Excellent Scientific and Technological Innovation Team of Jiangsu Province (2012) and Project for Jiangsu Scientific and Technological Innovation Team (2013).

Notes and references

[a]National Engineering Laboratory for Modern Silk, College of Textile and Clothing Engineering, Soochow University, Suzhou 215123, China.
[b]Research Center of Cooperative Innovation for Functional Organic / Polymer Material Micro/Nanofabrication, Soochow University, Suzhou, Jiangsu 215123, China.
[c]Petrochemical Research Chair, Department of Chemistry, College of Science, King Saud University, Riyadh 11451, Saudi Arabia.
[‡]These authors contributed equally to this publication.
Corresponding author email: jyhuang81@suda.edu.cn; kqzhang@suda.edu.cn; yklai@suda.edu.cn.

Electronic Supplementary Information (ESI) available: [The size distribution of Bi_2O_3 quantum dots and EDS spectra of Bi_2O_3@TiO_2 NTAs with multiple SILAR processes]. See DOI: 10.1039/b000000x/

1 A. Fujishima and K. Honda, *Nature*, 1972, **238**, 37-39.
2 a) K. Y. Lee, A. Mazare and P. Schmuki, *Chem. Rev.*, 2014, **114**, 9385-9454; b) I. Paramasivam, H. Jha, N. Liu, P. Schmuki, *Small*, 2012, **8**, 3073-3103; c) M. Y. Wang, J. Ioccozia, L. Sun, C. J. Lin and Z. Q. Lin, *Energy Environ. Sci.*, 2014, **7**, 2182-2202; d) M. Y. Wang, L. Sun, Z. Q. Lin, J. H. Cai, K. P. Xie and C. J. Lin, *Energy Environ. Sci.*, 2013, **6**, 1211-1220; e) G. H. Chen, S. Z. Ji, Y. H. Sang, S. J. Chang, Y. N. Wang, P. Hao, J. Claverie, H. Liu and G. Yu, *Nanoscale*, 2015, **7**, 3117-3125.
3 a) G. K. Mor, K. Shankar, M. Paulose, O. K. Varghese and C. A. Grimes, *Nano Lett.*, 2006, **6**, 215-218; b) J. Y. Hong, S. E. Bae, Y. S. Won and S. Huh, *J. Colloid Interf. Sci.*, 2015, **448**, 467-472; c) M. D. Ye, X. R. Wen, M. Y. Wang, J. Iocozzia, N. Zhang, C. J. Lin and Z. Q. Lin, *Mater. Today*, 2015, **18**, 155-162; d) Y. Wang, J. G. Yu, W. Xiao and Q. Li, *J. Mater. Chem. A*, 2014, **2**, 3847-3855.
4 a) Y. K. Lai, F. Pan, C. Xu, H. Fuchs and L. F. Chi, *Adv. Mater.*, 2013, **25**, 1682-1686; b) Y. K. Lai, L. X. Lin, F. Pan, J. Y. Huang, R. Song, Y. X. Huang, C. J. Lin, H. Fuchs and L. F. Chi, *Small*, 2013, **9**, 2945-2953; c) J. Y. Huang, Y. K. Lai, F. Pan, L. Yang, H. Wang, K. Q. Zhang, H. Fuchs and L. F. Chi, *Small*, 2014, **10**, 4865-4873; d) K. F. Huo, B. Gao, J. J. Fu, L. Z. Zhao and P. K. Chu, *RSC Adv.*, 2014, **4**, 17300-17324.
5 a) O. K. Varghese, D. W. Gong, M. Paulose, K. G. Ong, E. C. Dickey and C. A. Grimes, *Adv. Mater.*, 2003, **15**, 624-627; b) Y. F. Zhu, J. J. Shi, Z. Y. Zhang, C. Zhang and X. R. Zhang, *Anal. Chem.*, 2002, **74**, 120-124; c) K. F. Huo, Y. Li, R. S. Chen, B. Gao, C. J. Peng, W. J. Zhang, L. S. Hu, X. M. Zhang and P. K. Chu, *ChemPlusChem*, 2015, **80**, 576-582; d) Z. X. Yan, Z. H. Xu, J. G. Yu and G. Liu, *Electroanalysis*, 2014, **26**, 2017-2022.
6 a) S. K. Mohapatra, M. Misra, V. K. Mahajan and K. S. Raja, *J. Phys. Chem. C*, 2007, **111**, 8677-8685; b) M. D. Ye, J. J. Gong, Y. K. Lai, C. J. Lin and Z. Q. Lin, *J. Am. Chem. Soc.*, 2012, **134**, 15720-15723; c) Q. J. Xiang, J. G. Yu and M. Jaroniec, *J. Am. Chem. Soc.*, 2012, **134**, 6575-6578; d) X. Li, J. G. Yu, J. X. Low, Y. P. Fang, J. Xiao and X. B. Chen, *J. Mater. Chem. A*, 2015, **3**, 2485-2534.
7 a) X. B. Chen and S. S. Mao, *Chem. Rev.*, 2007, **107**, 2891-2959; b) U. Diebold, *Surf. Sci. Rep.*, 2003, **48**, 53-229.
8 a) Z. Liu, X. Zhang, S. Nishimoto, M. Jin, D. A. Tryk, T. Murakami and A. Fujishima, *J. Phys. Chem. C*, 2008, **112**, 253-259; b) Z. Liu, X. Zhang, S. Nishimoto, T. Murakami and A. Fujishima, *Environ. Sci. Technol.*, 2008, **42**, 8547-8551.
9 a) L. Sun, J. Li, C. L. Wang, S. F. Li, Y. K. Lai, H. B. Chen and C. J. Lin, *J. Hazard. Mater.*, 2009, **171**, 1045-1050; b) F. X. Xiao, S. F. Huang, J. W. Miao, H. Y. Wang, H. B. Yang and B. Liu, *Small*, 2015, **11**, 554-567; c) K. F. Huo, X. M. Zhang, H. R. Wang, L. Z. Zhao, X. Y. Liu and P. K. Chu, *Biomaterials*, 2013, **34**, 3467-3478; d) S. Pramanik, M. K. Mishra and G. De, *CrystEngComm*, 2014, **16**, 56-63.
10 a) X. Zhang, F. Wang, H. Huang, H. T. Li, X. Han, Y. Liu and Z. H. Kang, *Nanoscale*, 2013, **5**, 2274-2278; b) T. Nakajima, C. Y. Lee, Y. Yang and P. Schmuki, *J. Mater. Chem. A*, 2013, **1**, 1860-1866; c) Y. K. Lai, J. Y. Huang, H. F. Zhang, V. P. Subramaniam, Y. X. Tang, D. G. Gong, L. Sundar, L. Sun, Z. Chen and C. J. Lin, *J. Hazard. Mater.*, 2010, **184**, 855-863; d) L. S. Hu, K. F. Huo, R. S. Chen, B. Gao, J. J. Fu and P. K. Chu, *Anal. Chem.*, 2011, **83**, 8138-8144.
11 a) Y. Hou, X. Y. Li, X. J. Zou, X. Quan and G. H. Chen, *Environ. Sci. Technol.*, 2009, **43**, 858-863; b) L. Lin, Y. C. Yang, L. Men, X. Wang, D. N. He, Y. C. Chai, B. Zhao, S. Ghoshroy and Q. W. Tang, *Nanoscale*, 2013, **5**, 588-593; c) F. X. Xiao, J. W. Miao, H. Y. Miao, H. B. Yang, J. Z. Chen and B. Liu, *Nanoscale*, 2014, **6**, 6727-6737; d) M. N. Van, W. L. Li, P. T. Sheng, H. P. Van and Q. Y. Cai. *J. Electroanal. Chem.*, 2015, **736**, 69-75.
12 a) J. Zhang, S. Z. Qiao, L. F. Qi and J. G. Yu, *Phys. Chem. Chem. Phys.*, 2013, **15**, 12088-12094; b) J. Tian, Y. H. Sang, G. W. Yu, H. D. Jiang, X. N. Mu and H. Liu, *Adv. Mater.*, 2013, **25**, 5075-5080; c) J. Tian, Z. H. Zhao, A. Kumar, R. I. Boughtonc and H. Liu, *Chem. Soc. Rev.*, 2014, **43**, 6920-6937; d) J. Tian, Y. H. Sang, Z. H. Zhao, W. J. Zhou, D. Z. Wang, X. L. Kang, H. Liu, J. Y. Wang, S. W. Chen, H. Q. Cai and H. Huang, *Small*, 2013, **9**, 3864-3872.

13 a) H. Takeda, T. Ueda, K. Kamada, K. Matsuo, T. Hyodo and Y. Shimizu, *Electrochim. Acta*, 2015, **155**, 8-15; b) S. Park, H. Ko, S. Lee, H. Kim and C. Lee, *Thin Solid Films*, 2014, **570**, 298-302.
14 a) X. F. Liu, Y. K. Lai, J. Y. Huang, S. S. Al-Deyab and K. Q. Zhang, *J. Mater. Chem. C*, 2015, **3**, 345-351; b) L. Chen, J. He, Q. Yuan, Y. Liu, C. T. Au and S. F. Yin, *J. Mater. Chem. A.*, 2015, **3**, 1096-1102.
15 a) M. N. Gómez-Cerezo, M. J. Munoz-Batista, D. Tudela, M. Fernández-García and A. Kubacka, *Appl. Catal. B-Environ.*, 2014, **156**, 307-313; b) D. P. Dutta, M. Roy and A. K. Tyagi, *Dalton Trans.*, 2012, **41**, 10238-10248; c) Y. F. Qiu, M. L. Yang, H. B. Fan, Y. Z. Zuo, Y. Y. Shao, Y. J. Xu, X. X. Yang and S. H. Yang, *CrystEngComm*, 2011, **13**, 1843-1850.
16 a) L. Leontie, M. Caraman, M. Delibas and G. I. Rusu, *Mater. Res. Bull.*, 2001, **36**, 1629; b) B. Yang, M. Mo, H. Hu, C. Li, X. Yang, Q. Li and Y. T. Qian, *Eur. J. Inorg. Chem.*, 2004, **9**, 1785-1787; c) L. Zhou, W. Z. Wang, H. L. Xu, S. M. Sun and M. Shang, *Chem. Eur. J.*, 2009, **15**, 1776-1782.
17 M. Schlesinger, S. Schulze, M. Hietschold and M. Mehring, *Dalton Trans.*, 2013, **42**, 1047-1056.
18 a) J. Y. Zhang, W. Q. Dang, X. C. Yan, M. Li, H. Gao and Z. M. Ao, *Phys. Chem. Chem. Phys.*, 2014, **16**, 23476-23482; b) H. F. Cheng, B. B. Huang, J. B. Lu, Z. Y. Wang, B. Xu, X. Y. Qin, X. Y. Zhang and Y. Dai, *Phys. Chem. Chem. Phys.*, 2010, **12**, 15468-15475; c) K. Brezesinski, R. Ostermann, P. Hartmann, J. Perlich and T. Brezesinski, *Chem. Mater.*, 2010, **22**, 3079-3085; d) L. F. Yin, J. F. Niu, Z. Y. Shen and J. Chen, *Environ. Sci. Technol.*, 2010, **44**, 5581-5586.
19 Z. H. Zhao, J. Tian, D. Z. Wang, X. L. Kang, Y. H. Sang, H. Liu, J. Y. Wang, S. W. Chen, R. I. Boughtond and H. D. Jiang, *J. Mater. Chem.*, 2012, **22**, 23395-23403.
20 X. Zhao, H. J. Liu and J. H. Qu, *Appl. Surf. Sci.*, 2011, **257**, 4621-4624.
21 a) J. Zhu, S. H. Wang, J. G. Wang, D. Q. Zhang and H. X. Li, *Appl. Catal. B-Environ.*, 2011, **102**, 120-125; b) M. Ge, Y. F. Li, L. Liu, Z. Zhou and W. Chen, *J. Phys. Chem. C*, 2011, **115**, 5220-5225; c) Y. Wang, S. K. Li, X. R. Xing, F. Z. Huang, Y. H. Shen, A. J. Xie, X. F. Wang and J. Zhang, *Chem.-Eur. J.*, 2011, **17**, 4802-4808.
22 Y. Cong, J. L. Zhang, F. Chen and M. Anpo, *J. Phys. Chem. C*, 2007, **111**, 6976-6982.
23 D. Y. Li, Y. G. Zhang, Y. L. Zhang, X. F. Zhou and S. J. Guo, *J. Hazard. Mater.*, 2013, **258-259**, 42-49.
24 a) J. G. Hou, C. Yang, Z. Wang, S. Q. Jiao and H. M. Zhu, *Appl. Catal. B-Environ.*, 2013, **129**, 333-341; b) J. G. Hou, Z. Wang, S. Q. Jiao and H. M. Zhu, *J. Hazard. Mater.*, 2011, **192**, 1772-1779; c) J. G. Hou, Z. Wang, S. Q. Jiao and H. M. Zhu, *CrystEngComm*, 2012, **14**, 5923-5928.
25 G. P. Dai, J. G. Yu and G. Liu, *J. Phys. Chem. C*, 2011, **115**, 7339-7346.
26 a) J. Q. Liu, L. L. Ruan, S. B. Adeloju and Y. C. Wu, *Dalton Trans.*, 2014, **43**, 1706-1715; b) Y. Peng, M. Yan, Q. G. Chen, C. M. Fan, H. Y. Zhou and A. W. Xu, *J. Mater. Chem. A*, 2014, **2**, 8517-8524; c) H. Y. Jiang, P. Li, G. G. Liu, J. H. Ye and J. Lin, *J. Mater. Chem. A*, 2015, **3**, 5119-5125; d) B. C. Weng, F. H. Xu and J. G. Xu, *RSC Adv.*, 2014, **4**, 56682-56689.
27 a) J. Guo, W. Fu, H. Yang, Q. Yu, W. Zhao, X. Zhou, Y. Sui, J. Ding, Y. Li, S. Cheng and M. Li, *J. Phys. D*, 2010, **43**, 245202; b) G. K. Mor, H. E. Prakasam, O. K. Varghese, K. Shankar and C. A. Grimes, *Nano Lett.*, 2007, **7**, 2356-2364; c) A. Fuerte, M. D. Hernandez-Alonso, A. J. Maira, A. Martinez-Arias, M. Fernandez-Garcıa, J. C. Conesa, J. Soria and G. Munuera, *J. Catal.*, 2002, **212**, 1-9.
28 a) Z. Bian, J. Zhu, S. Wang, Y. Cao, X. Qian and H. Li, *J. Phys. Chem. C*, 2008, **112**, 6258-6262; b) S. S. Yi, X. Z. Yue, D. D. Xu, Z. P. Liu, F. Zhao, D. J. Wang and Y. H. Lin, *New J. Chem.*, 2015, **39**, 2917-2924.
29 a) G. K. Mor, H. E. Prakasam, O. K. Varghese, K. Shankar and C. A. Grimes, *Nano Lett.*, 2007, **7**, 2356-2364; b) Z. Wu, Y. Y. Wang, L. Sun, Y. X. Mao, M. Y. Wang and C. J. Lin, *J. Mater. Chem. A*, 2014, **2**, 8223-8229.
30 a) N. Serpone, D. Lawless and R. Khairutdinov, *J. Phys. Chem.*, 1995, **99**, 16646-16654; b) Y. Zhang, X. Li, X. Hua, N. Ma, D. Chen and H. Wang, *Scr. Mater.*, 2009, **61**, 296-299.
31 a) X. T. Wang, C. H. Liow, A. Bisht, X. F. Liu, T. C. Sum, X. D. Chen and S. Z. Li, *Adv. Mater.*, 2015, **27**, 2207-2214; b) Y. Y. Zhang, Y. X. Tang, X. F. Liu, Z. L. Dong, H. H. Hng, Z. Chen, T. C. Sum and X. D. Chen, *Small*, 2013, **9**, 996-1002.
32 M. Z. Ge, S. H. Li, J. Y. Huang, K. Q. Zhang, S. S. Al-Deyab and Y. K. Lai, *J. Mater. Chem. A*, 2015, **3**, 3491-3499.
33 a) M. Y. Wang, D. J. Zheng, M. D. Ye, C. C. Zhang, B. B. Xu, C. J. Lin, L. Sun and Z. Q. Lin, *Small*, 2015, **11**, 1436-1442; b) X. T. Wang, C. H. Liow, D. P. Qi, B. W. Zhu, W. R. Leow, H. Wang, C. Xue, X. D. Chen and S. Z. Li, *Adv. Mater.*, 2014, **26**, 3506-3512.
34 Y. Peng, M. Yan, Q. G. Chen, C. M. Fan, H. Y. Zhou and A. W. Xu, *J. Mater. Chem. A*, 2014, **2**, 8517-8524.
35 Z. Zhang, C. Shao, X. Li, C. Wang, M. Zhang and Y. Liu, *ACS Appl. Mater. Interfaces*, 2010, **2**, 2915-2923.

Graphical Abstract:

An ultrasonication-assisted successive ionic layer adsorption and reaction (SILAR) strategy was developed to uniformly deposit p-type Bi_2O_3 quantum dots on n-type TiO_2 nanotube arrays for greatly enhanced photocatalytic activity.